

Research Article

Online Measuring and Size Sorting for Perillae Based on Machine Vision

Bo Zhao,¹ Ye Wang,¹ Jun Fu ,^{1,2} Rongqiang Zhao ,² Yashuo Li,¹ Xin Dong,¹ Chengxu Lv,¹ and Hanlu Jiang¹

¹Chinese Academy of Agricultural Mechanization Sciences, Beijing 100083, China

²College of Biological and Agricultural Engineering, Jilin University, Changchun 130022, China

Correspondence should be addressed to Jun Fu; fu_jun@jlu.edu.cn

Received 18 September 2019; Accepted 31 October 2019; Published 13 January 2020

Guest Editor: Yuan Li

Copyright © 2020 Bo Zhao et al. This is an open access article distributed under the Creative Commons Attribution License, which permits unrestricted use, distribution, and reproduction in any medium, provided the original work is properly cited.

Perillae has attracted an increasing interest of study due to its wide usage for medicine and food. Estimating quality and maturity of a perillae requires the information with respect to its size. At present, measuring and sorting the size of perillae mainly depend on manual work, which is limited by low efficiency and unsatisfied accuracy. To address this issue, in this study, we develop an approach based on the machine vision (MV) technique for online measuring and size sorting. The geometrical model and the corresponding mathematical model are built for perillae and imaging, respectively. Based on the built models, the measuring and size sorting method is proposed, including image binarization, key point determination, information matching, and parameter estimation. Experimental results demonstrate that the average time consumption for a captured image, the average measuring error, the variance of measuring error, and the overall sorting accuracy are 204.175 ms, 1.48 mm, 0.07 mm, and 93%, respectively, implying the feasibility and satisfied accuracy of the proposed approach.

1. Introduction

Perillae is widely distributed throughout Asia, and it has attracted an increasing interest in the field of medicine and pharmacy. Perillae has been applied for bacteriostatic, detoxifying, antitussive, and phlegm for thousands of years in traditional Chinese medicine. Recently, more attentions have been paid to the study with respect to perillae, including the perillae herba ethanolic [1], the luteolin [2], and the rosmarinic acid [3]. Besides, perillae is also a popular food in countries such as China, Japan, and Korea. The size of perillae indicates its quality and maturity that closely relates to its medical and edible value. Hence, it is of great significance to measure and sort the size of perillae in advance. At present, measuring and sorting the size of perillae mainly depend on manual work, which is of low efficiency and unsatisfied accuracy. Therefore, it is valuable to develop an approach for accurate online measurement and sort of perillae.

Machine vision (MV) is the technique to provide imaging-based automatic inspection [4–6], and it has been widely used in the fields of industry, such as object detection and robot guidance [7, 8]. For the applications in agriculture, previous work has explored into various crops [9, 10]. In [11], a compact machine vision system based on hyperspectral imaging and machine learning is presented to detect aflatoxin in chili pepper. In [12], a hierarchical grading method is applied for real-time defect detection and size sorting of potatoes. In [13], a study is conducted to predict ripening quality in mangoes using RGB images, for which the hierarchical clustering method is employed to classify the ripening period into five stages based on quality parameters. In [14], the authors combine the MV and the support vector machine to develop an intelligent system for sorting of peeled pistachio kernels and shells. In [15], Sabliov et al. develop an MV-based method to measure volume and surface area of ellipsoidal agricultural products by regarding the objects as

the sum of superimposed elementary frustums of right circular cones. In [16], Yao et al. develop real-time detection instrumentation for aflatoxin-contaminated corn using a narrow-band fluorescence index. In [17], Pedreschi et al. present an inexpensive computer vision system for measuring the color of a highly heterogeneous food material such as potato chips. In [18], Huang et al. propose an approach for identification of defect pleurotus geesteranus based on computer vision. In [19], Sun et al. develop a machine vision system and the dynamic weighing system for the measurement of egg external physical characteristic and weight, such that the nondestructive method for online estimation of egg freshness is achieved. Additionally, a set of studies have been conducted on measurement, cabbage [20], flower mushroom [21], cherry [22], litchi [23], and other agricultural products [24–29].

However, the automatic online detection of perillae has not been explored till now. The geometry model and the corresponding mathematical model of perillae used for automatic detection have not been built yet. The size sorting of perillae still requires manual work. To address this issue, in this study, we develop a novel approach for online measuring and size sorting of perillae. A charge-coupled device (CCD) camera is employed to acquire the images of perillae in the lighting box, and the MV method is proposed for image processing. The contributions of this study can be summarized as follows.

- (1) We build the general geometry model of perillae and the corresponding mathematical model for image processing
- (2) We propose the MV-based method for accurate online measuring and size sorting of perillae under the proposed models
- (3) We develop the practical system for our theoretical method, the feasibility and accuracy of which are verified by the experimental results

The remainder of this paper is organized as follows. Section 2 introduces the proposed geometry model and mathematical model. Section 3 provides the MV-based online measuring method. Section 4 presents the experimental results and analysis. Section 5 concludes this paper.

2. Geometry and Mathematical Models

2.1. Geometry Model. Figure 1 shows a typical perillae for medical and food usage. The notation L_u is used to denote the length of a perillae, i.e., the maximum size of perillae leaf. We mainly consider the length between P_A and P_B as it is the useful part of perillae, regardless of the medical or food usage. The length between P_B and P_C , i.e., the length of perillae, is not taken into the measurement.

Figure 2 presents the sorting principle for the size of perillae. In this study, the sizes are divided into four grades according to L_u . As shown in Figure 2, the first grade is expressed as “Spec M” with the size of $7\text{ cm} \leq L_u < 8.5\text{ cm}$, denoting the smallest perillae. The second grade, “Spec

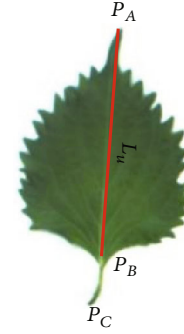


FIGURE 1: Geometry model of perillae where P_A , P_B , and P_C represent the apex of perillae, the separation point of leaf and petiole, and the endpoint of petiole, respectively.

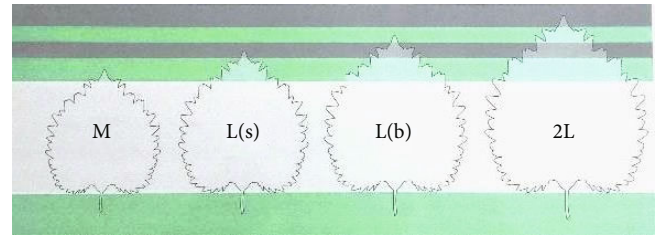


FIGURE 2: Classification of perillae sizes.



FIGURE 3: Classification of perillae sizes.

“L(s),” and the third grade, “Spec L(b),” are determined by $8.5\text{ cm} \leq L_u < 9.5\text{ cm}$ and $9.5\text{ cm} \leq L_u < 10.5\text{ cm}$, respectively. The fourth grade, expressed as “Spec 2M,” is used to represent the largest size, given by $10.5\text{ cm} \leq L_u < 12\text{ cm}$.

2.2. Mathematical Model. Next, we provide the mathematical model for imaging of perillae. The camera used in this study was calibrated before it is employed for imaging. As shown in Figure 3, we captured 20 chessboard images with different poses and then utilized the calibration tool in the OpenCV to calibrate the camera.

Let u , v , and w denote the horizontal coordinate, the vertical coordinate, and the position perpendicular to the chessboard in the camera coordinate, respectively, and let x , y , and z denote the corresponding coordinates in the world coordinate. The calibration results demonstrate the distortion error, and the reprojection error can be ignored. Assume $M(x, y, z)$ is a pixel in the world coordinate system, and this pixel is then projected into the camera coordinate system, expressed

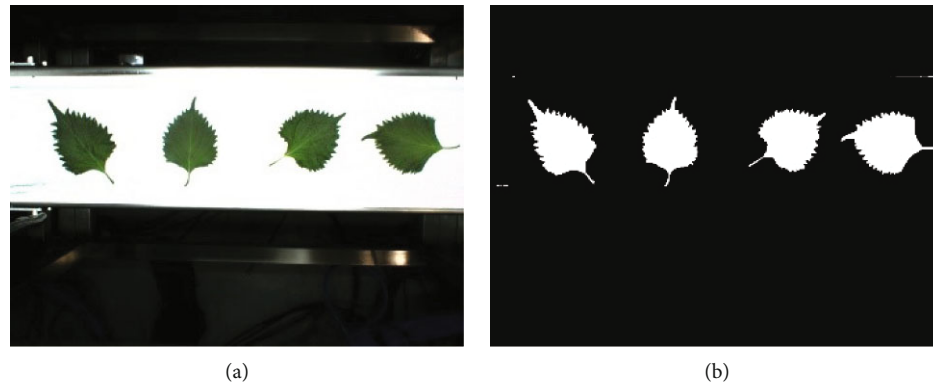


FIGURE 4: Image binarization.

as $m(u, v)$. Let \mathbf{G} be the intrinsic matrix of the used camera. Based on the used calibration tool, the transformation between the world coordinate system and the camera coordinate system can be expressed as

$$\begin{bmatrix} u \\ v \\ w \end{bmatrix} = \mathbf{G} \begin{bmatrix} x \\ y \\ z \end{bmatrix}. \quad (1)$$

The matrix \mathbf{G} is obtained through the calibration, and the result is

$$\mathbf{G} = \begin{bmatrix} \frac{1}{\alpha_x} & 0 & \frac{1}{\beta_x} \\ 0 & \frac{1}{\alpha_y} & \frac{1}{\beta_y} \\ 0 & 0 & 1 \end{bmatrix} = \begin{bmatrix} \frac{1}{1345.538} & 0 & \frac{1}{606.253} \\ 0 & \frac{1}{1345.538} & \frac{1}{470.283} \\ 0 & 0 & 1 \end{bmatrix}. \quad (2)$$

By combining the geometrical model and (2), we can rewrite the size of perillae as follows:

$$\begin{aligned} L_u &= \sqrt{(p_{A,x} - p_{B,x})^2 + (p_{A,y} - p_{B,y})^2} \\ &= \sqrt{\left(\frac{q_{A,x} - q_{B,x}}{\alpha_x}\right)^2 + \left(\frac{q_{A,y} - q_{B,y}}{\alpha_y}\right)^2}, \end{aligned} \quad (3)$$

where $p_{A,x}$, $p_{A,y}$, $p_{B,x}$, and $p_{B,y}$ are the coordinates of points P_A and P_B in the world coordinate system and $q_{A,x}$, $q_{A,y}$, $q_{B,x}$, and $q_{B,y}$ are the coordinates of points P_A and P_B in the image coordinate system. Obviously, the required size can be calculated out directly if parameter z and the coordinates of P_A and P_B are known. Hence, we introduce the proposed method to determine this information in the next section.

3. Method for Measuring Perillae

In this section, we provide the proposed method for measuring and size sorting of perillae based on the MV and the proposed models. The method is composed of the following steps, binarizing the original image, determining the positions of P_A and P_B , matching information, and estimating parameter z .

3.1. Image Binarization. Figure 4(a) presents the original image of perillae. The image should be binarized before it is used for measuring. The binarization principle is given by

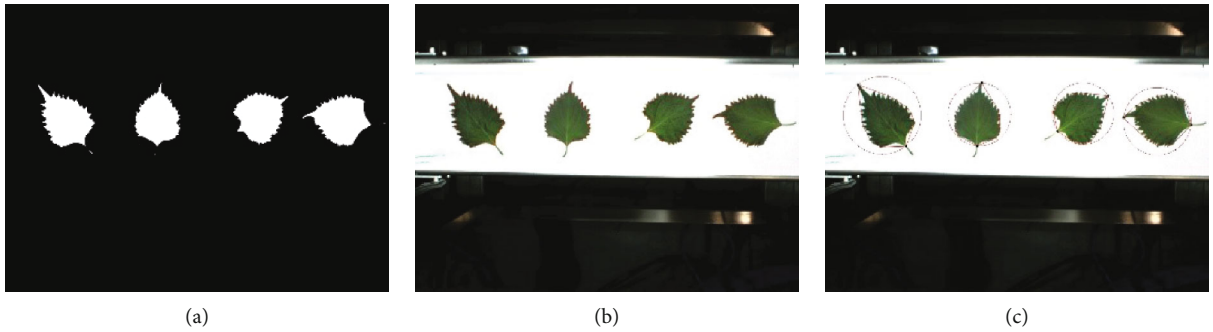
$$j(x, y) = \begin{cases} 255, & 380 \leq y \leq 690, h_b < 180, h_r < 220, \\ 0, & \text{otherwise,} \end{cases} \quad (4)$$

where $j(x, y)$ is the value of the pixel (x, y) in the binarized image. The depth of the image is 8 bits, and therefore, the value of white pixels is set to 255. As indicated in (4), a pixel is determined to be white as long as $380 \leq y \leq 690$, $h_b < 180$, and $h_r < 220$, where h_b and h_r are the values of the pixel in the blue channel and the red channel, respectively. The first condition, $380 \leq y \leq 690$, ensures that the background is set to be black, and only the area containing perillae is considered. The second and the third conditions are utilized to determine whether a pixel belongs to the area of perillae. The binarized image is shown as Figure 4(b).

3.2. Search for P_A . We first derive the contour from the binarized image. The strategy is to set the thresholds for the largest and the smallest areas of the perillae. Thus, the areas that satisfy the constraint of thresholds are selected, and their contours are regarded as the contours of perillae. This process can be expressed as

$$cjr_i = \begin{cases} 1, & 6000 < A_i < 30000, \\ 0, & \text{otherwise,} \\ 1 \leq i \leq N \end{cases} \quad (5)$$

where N denotes the total number of contours in the binarized image, A_i denotes the area of the i^{th} contours, and cjr_i

FIGURE 5: Determination of P_A .FIGURE 6: Determination of P_B .

is the judging result. Then, the minimum enclosing circle and the convex hull of each perillae can be obtained. These perillae are labelled as 1, 2, 3, and 4 from left to right based on the following judgement:

$$pjr_j = \begin{cases} 1, & 1 \leq c_{j,x} \leq 320, \\ 2, & 321 \leq c_{j,x} \leq 640, \\ 3, & 641 \leq c_{j,x} \leq 960, \\ 4, & 961 \leq c_{j,x} \leq 1280, \\ 1 \leq j \leq \text{Num1}, \end{cases} \quad (6)$$

where pjr_j is the judgement for each position of perillae, $c_{j,x}$ denotes the horizontal coordinate of the center of the j^{th} enclosing circle, and “Num1” denotes the amount of perillae in the captured image. The results are displayed in Figure 5(b) and are saved as “Pos1.”

Finally, we utilize the following strategy to find the endpoints of the l^{th} contours, written as $p_{11,l}$ and $p_{12,l}$:

$$p_{11,l} = \arg \min_{cp_{l,k}} \text{abs} \left(\sqrt{(cp_{l,k,x} - cc_{l,x})^2 + (cp_{l,k,y} - cc_{l,y})^2} - r_l \right), \quad (7)$$

$$1 \leq l \leq \text{Num1}, 1 \leq k \leq m_l,$$

$$p_{12,l} = \arg \min_{cp_{l,k}} \sqrt{(cp_{l,k,x} - p_{11,l,x})^2 + (cp_{l,k,y} - p_{11,l,y})^2}, \quad (8)$$

$$1 \leq l \leq \text{Num1}, 1 \leq k \leq m_l - 1,$$

where $cp_{l,k}$ denotes the k^{th} pixel in the l^{th} convex hull, $cp_{l,k,x}$ and $cp_{l,k,y}$ are the coordinates of $cp_{l,k}$, $cc_{l,x}$ and $cc_{l,y}$ are the coordinates of the center of the l^{th} enclosing circle, r_l represents the radius of the l^{th} enclosing circle, and m_l is the amount of pixels of the l^{th} convex hull. In fact, $p_{11,l}$ can be regarded as the point furthest away from the center of the enclosing circle, and $p_{12,l}$ is the point furthest away from $p_{11,l}$. These two points are generally P_A and P_C . The data of “Num1,” “Pos1,” p_{11} , and p_{12} are saved as “Info1.”

3.3. Search for P_B . To acquire the position of P_B , we conduct one close operation, four erode operations, and four dilate operations in the OpenCV for the binarized image, successively. The results are presented in Figure 6(a). Then, we derive the treated contours using the strategy given by (7) and (8). The results are shown in Figure 6(b) and are saved as “Pos2.” Finally, the minimum enclosing circle and the convex hull of the derived contours are obtained, shown as Figure 6(c). Similar to the procedure to search for P_A and P_C , two endpoints, p_{21} and p_{22} , are selected as the alternative

points of P_B . The other one is defined as P_D . The data of “Pos2,” p_{21} , and p_{22} are saved into “Info2.”

3.4. Information Matching. Next, we should recognize P_A and P_B from p_{11} , p_{12} , p_{21} , and p_{22} . For this purpose, we first compute the Euclidean distance from p_{21} to p_{11} , p_{21} to p_{12} , p_{22} to p_{11} , and p_{22} to p_{12} , respectively. Then, we compare the four distances and find out the two points that lead to the largest distance. Assuming the two points are p_{12} and p_{22} , we can draw the conclusion that P_C is p_{12} , as p_{12} is the alternative point of P_A and P_C , and the distance from P_C to P_D is always larger than that of P_A to P_B . Repeat the procedure for all “Num1” contours of perillae, such that the position of P_A and P_B of each perillae can be obtained. We summarize all four possibilities in Table 1.

3.5. Scale Factor Estimation and Size Computation. As indicated in (8), parameter z is the factor controlling the scale of imaging. Hence, we utilize the following scale method to estimate z . As shown in Figure 7, the original plane is $z = c_2$. We use A_2B_2 to represent the manual measurement and use A_0B_0 to represent the corresponding measurement in the camera coordinate system. Then, we manually set z to c_1 to acquire the measurement A_1B_1 by using (8). Based on these measurements, we have

$$\frac{A_0B_0}{A_1B_1} = \frac{f}{c_1}, \quad (9)$$

$$\frac{A_0B_0}{A_2B_2} = \frac{f}{c_2}. \quad (10)$$

Therefore, z can be calculated by

$$z = c_2 = \frac{A_2B_2}{A_1B_1}. \quad (11)$$

To eliminate the measurement error, we repeat the above process for 20 times, and the average value is used for the experiments, computed by

$$z = c_2 = \frac{\sum_{i=1}^{20} c_{2i}}{20}, \quad (12)$$

where c_{2i} denotes the calculated value in the i^{th} trial.

The proposed approach is summarized in Figure 8.

4. Experimental Results

Our experimental system is shown in Figure 9, composed of a lighting box and a personal computer (PC). The lighting box contains four light-emitting diode (LED) light located as a ring on the top of the box and a CCD camera in the center of the box. The experimental setup is described as follows. Before conducting the experiments, we manually set $c_1 = 50$ cm and obtain $z = 68.765$ cm by using the strategy introduced in Subsection 3.5. This value of z is used for all experiments in this study. First, we randomly chose 100 perillae

TABLE 1: Information matching, P_A and P_B to p_{11} , p_{12} , p_{21} , and p_{22} .

Points leading to the largest distance	P_A	P_B
p_{11} and p_{21}	p_{12}	p_{22}
p_{11} and p_{22}	p_{12}	p_{21}
p_{12} and p_{21}	p_{11}	p_{22}
p_{12} and p_{22}	p_{11}	p_{21}

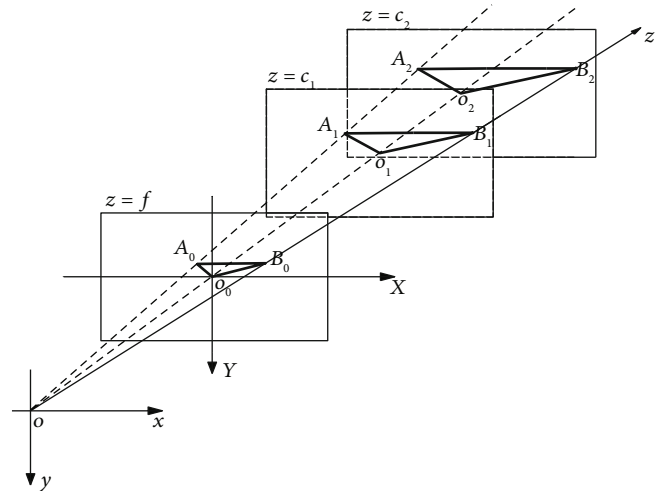


FIGURE 7: Pinhole imaging model.

and manually measured their sizes. Then, we used the developed system to measure these perillae.

The results by both manual measurement and automatic online measurement are presented in Figure 10. We computed the measurement error for each perillae, and the results are provided in Figure 11. Obviously, the results obtained by online measurement are close to those obtained by manual measurement. As provided in Table 2, among the 100 perillae, the maximum measuring error (MAME) is 3.66 mm, while the minimum measuring error (MIME) is 0.02 mm. Most of the errors are lower than 3 mm. The overall average measuring error (OAME) and the variance of measuring error (VME) are 1.47 mm and 0.07 mm, respectively.

5. Conclusions

We developed an MV-based approach for automatic measuring and size sorting of perillae. We first built the geometric model for perillae and the mathematical model for imaging. Based on the models, the measuring and size sorting method was proposed, including image binarization, key point determination, information matching, and parameter estimation. We employed the CCD camera for imaging and the OpenCV tools for image processing. Experimental results have verified the feasibility of our system and its high accuracy of measuring and size sorting. By using 100 perillae for experiments, the MAME and the MIME are 3.66 mm and 0.02 mm, respectively. Most of the errors are lower than 3 mm. The OAME

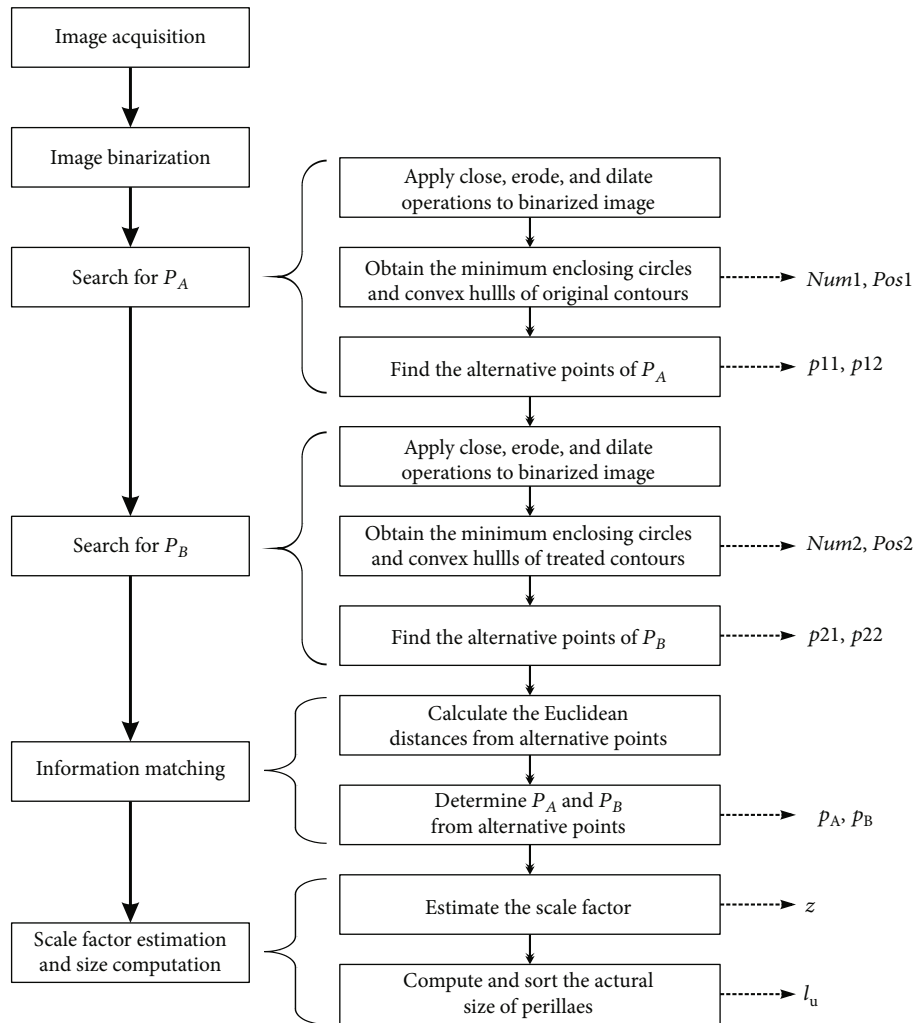


FIGURE 8: Outline of the proposed approach.

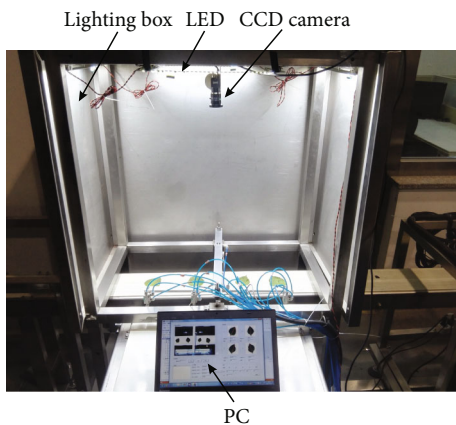


FIGURE 9: Experimental system.

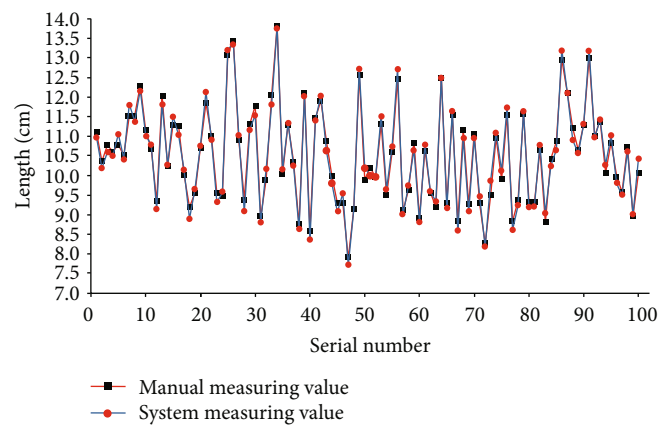


FIGURE 10: Measuring result.

and the VME are 1.47 mm and 0.07 mm, respectively. Further study could address on the following issues. First, miniaturization for the developed system requires future work to

make the proposed approach more particle. Second, utilizing the RGB image or hyperspectral image to detect the maturity of perillae is also valuable for further study.

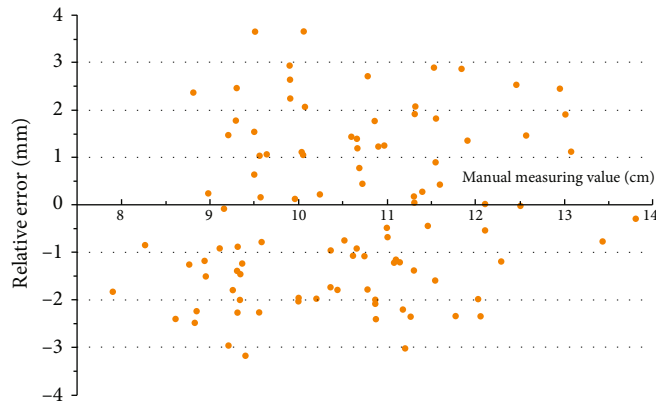


FIGURE 11: Measuring error for each perillae.

TABLE 2: Overall measuring and sorting results.

	ATCCI (ms)	MAME (mm)	MIME (mm)	OAME (mm)	VME (mm)	OSA (%)
Results	204.175	3.66	0.02	1.47	0.07	93

Data Availability

The data used to support the findings of this study are available from the corresponding author upon request.

Conflicts of Interest

The authors claim no conflicts of interest.

Acknowledgments

This work was supported by the National Key Research and Development Project under Grant 2017YFD0401305.

References

- [1] J. Yang, J. Yoo, E. Lee et al., "Anti-inflammatory effects of Perillae Herba ethanolic extract against TNF- α /IFN- γ -stimulated human keratinocyte HaCaT cells," *Journal of Ethnopharmacology*, vol. 211, pp. 217–223, 2018.
- [2] X. Kong, G. Huo, S. Liu, F. Li, W. Chen, and D. Jiang, "Luteolin suppresses inflammation through inhibiting cAMP-phosphodiesterases activity and expression of adhesion molecules in microvascular endothelial cells," *Inflammopharmacology*, vol. 27, no. 4, pp. 773–780, 2019.
- [3] N. Ito, T. Yabe, Y. Gamou et al., "Rosmarinic acid from perillae herba produces an antidepressant-like effect in mice through cell proliferation in the hippocampus," *Biological and Pharmaceutical Bulletin*, vol. 31, no. 7, pp. 1376–1380, 2008.
- [4] V. G. Narendra and K. S. Hareesh, "Quality inspection and grading of agricultural and food products by computer vision - a review," *International Journal of Computer Applications*, vol. 2, no. 1, pp. 43–65, 2010.
- [5] B. Zhang, W. Huang, J. Li et al., "Principles, developments and applications of computer vision for external quality inspection of fruits and vegetables: a review," *Food Research International*, vol. 62, no. 62, pp. 326–343, 2014.
- [6] Y. Chen, K. Chao, and M. S. Kim, "Machine vision technology for agricultural applications," *Computers and Electronics in Agriculture*, vol. 36, no. 2-3, pp. 173–191, 2002.
- [7] T. Brosnan and D. Sun, "Inspection and grading of agricultural and food products by computer vision systems—a review," *Computers and Electronics in Agriculture*, vol. 36, no. 2-3, pp. 193–213, 2002.
- [8] H. S. El-Mesery, H. Mao, and A. E. F. Abomohra, "Applications of non-destructive technologies for agricultural and food products quality inspection," *Sensors*, vol. 19, no. 4, p. 846, 2019.
- [9] Y. Ying, X. Rao, Y. Zhao, and J. YiYuan, "Application of machine vision technique to automatic quality identification of agricultural products (I)," *Transactions of the Chinese Society of Agricultural Engineering*, vol. 16, no. 3, pp. 103–108, 2000.
- [10] N. Zhao, P. Zhao, and Y. Gao, "Study on application of machine vision technology to modern agriculture in China," *Journal of Tianjin Agricultural University*, vol. 22, pp. 55–58, 2015.
- [11] M. Atas, Y. Yardimci, and A. Temizel, "A new approach to aflatoxin detection in chili pepper by machine vision," *Computers and Electronics in Agriculture*, vol. 87, pp. 129–141, 2012.
- [12] N. Razmjoooy, B. S. Mousavi, and F. Soleymani, "A real-time mathematical computer method for potato inspection using machine vision," *Computers & Mathematics with Applications*, vol. 63, no. 1, pp. 268–279, 2012.
- [13] V. N. Eyarkai, K. Thangave, S. Shahir, and V. Thirupathi, "Comparison of various RGB image features for nondestructive prediction of ripening quality of "alphonso" mangoes for easy adoptability in machine vision applications: a multivariate approach," *Journal of Food Quality*, vol. 39, no. 6, 825 pages, 2016.
- [14] H. Nouri-Ahmadabadi, M. Omid, S. S. Mohtasebi, and M. Soltani Firouz, "Design, development and evaluation of an online grading system for peeled pistachios equipped with machine vision technology and support vector machine," *Information Processing in Agriculture*, vol. 4, no. 4, pp. 333–341, 2017.
- [15] C. M. Sabliov, D. Boldor, K. M. Keener, and B. E. Farkas, "Image processing method to determine surface area and volume of axi-symmetric agricultural products," *International Journal of Food Properties*, vol. 5, no. 3, pp. 641–653, 2002.
- [16] H. Yao, Z. Hruska, R. Kincaid et al., "Development of narrow-band fluorescence index for the detection of aflatoxin contaminated corn," in *Conference on the Sensing for Agriculture and Food Quality and Safety III*, vol. 8027, Orlando, Florida, United States, APRIL 2011.
- [17] F. Pedreschi, J. Leon, D. Mery, and P. Moyano, "Development of a computer vision system to measure the color of potato chips," *Food Research International*, vol. 39, no. 10, pp. 1092–1098, 2006.
- [18] X. Huang, S. Jiang, Q. Chen, and Z. Jiwen, "Identification of defect pleurotus geesteranus based on computer vision," *Transactions of the Chinese Society of Agricultural Engineering*, vol. 26, no. 10, pp. 350–354, 2010.
- [19] L. Sun, L. Yuan, J. Cai, H. Lin, and J. W. Zhao, "Egg freshness on-line estimation using machine vision and dynamic weighing," *Food Analytical Methods*, vol. 8, no. 4, pp. 922–928, 2015.

- [20] H. Li, H. Sun, and M. Li, "Identification of cabbage ball shape based on machine vision," *Transactions of the Chinese Society for Agricultural Machinery*, vol. s1, pp. 141–146, 2015.
- [21] H. Chen, Q. Xia, T. Zuo, T. HeQun, and B. YinBing, "Determination of shiitake mushroom grading based on machine vision," *Nongye Jixie Xuebao*, vol. 45, no. 1, pp. 281–287, 2014.
- [22] W. Hui, L. Yuchun, K. Feng, W. Qi, Z. Bo, and Z. Qin, "Size detection for cherry fruit based on machine vision," *Transactions of the Chinese Society for Agricultural Machinery*, vol. 43, no. s1, pp. 246–249, 2012.
- [23] J. Xiong, X. Zou, N. Liu, P. HongXing, L. JinHong, and L. GuiChao, "Fruit quality detection based on machine vision technology when picking litchi," *Nongye Jixie Xuebao*, vol. 45, no. 7, pp. 54–60, 2014.
- [24] F. Zhang, S. Li, and Z. Liu, "Screening method of abnormal corn ears based on machine vision," *Transactions of the Chinese Society for Agricultural Machinery*, vol. 46, pp. 45–49, 2015.
- [25] Z. Ping, Z. ChunJiang, W. JiHua, Z. Wen'gang, S. ZhongFu, and W. YouXian, "Egg geometry calculations based on machine vision," *Nongye Jixie Xuebao*, vol. 41, pp. 168–171, 2010.
- [26] H. Wang, J. Xiong, Z. Li, J. Deng, and X. Zou, "Potato grading method of weight and shape based on imaging characteristic parameters in machine vision," *Transactions of the Chinese Society of Agricultural Engineering*, vol. 32, no. 8, pp. 272–277, 2016.
- [27] W. Wei, Y. Xing, Y. Li, Y. Peng, and W. Zhang, "Online detection and classification system of external quality of leaf for dining hall and family," *Transactions of the Chinese Society of Agricultural Engineering*, vol. 34, no. 5, pp. 264–273, 2018.
- [28] L. Li, Y. Peng, and Y. Li, "Design and experiment on grading system for online non-destructive detection of internal and external quality of apple," *Transactions of the Chinese Society of Agricultural Engineering*, vol. 34, no. 9, pp. 267–273, 2018.
- [29] G. Wang, L. Sun, X. Li, M. Zhang, Q. Lyu, and J. Cai, "Design of postharvest in-field grading system for navel orange based on machined vision," *Journal of Jiangsu University*, vol. 38, no. 6, pp. 672–676, 2017.

